Reduction Reactions of CO₂ on Rutile TiO₂ (110) Nanosheet via Coordination Activation

Xuemei Yang* and Xiaohua Wang
School of Chemical and Environmental Engineering, Jiaozuo University,
3066 Renmin Road, Jiaozuo, Henan Province, China. Postcode 454000
yxm06102021@163.com*

Summary: Based on the previous coordination catalysis theory, the active site on the surface of transition metal oxides can activate the CO_2 molecule. Ultrathin two-dimensional (2D) rutile TiO_2 nanosheet with (110) crystal face as the main exposed surface has many active sites of Ti^{3+} and O vacancy, which have some synergistic effects to greatly reduce the dissociation energy of CO_2. Following previous assumptions, four possible reduction processes of CO_2 on rutile TiO_2 (110) surface were systematically assessed by density functional theory (DFT) simulations. The reduction reactions of CO_2 along I faces difficultly in proceeding due to the relatively weak interaction between CO_2 and the active surface. Additionally, along III, the adsorption configuration of CO_2 in the pristine state has huge distinctions with the model that suggests that the defined route is unlikely to occur on the rutile TiO_2 (110) surface. However, through carefully comparing the energy differences as well as transition state searching, the reduction reaction along II has a high probability of finishing and finally generating HCOOH on the surface owing to the minimal energy differences and low activation barrier. Furthermore, the reduction reaction of CO_2 to CH_4 guided along IV is predicted to more easily take place with the assistance of O vacancy on the active surface. The synergistic action among Ti^{3+} site, O vacancy, and H^+ can aid in fixing molecular CO_2 by breaking the strong bond of C=O in CO_2 and generating different fuels via coordination activation. This work will not only provide strong theoretical support to previous assumptions but can also lighten the routes to explore more active catalysis towards the reduction of CO_2.

Keywords: Reduction, CO_2, DFT, Rutile TiO_2, (110) nanosheet, Coordination activation.

Introduction

To address issues stemming from the greenhouse effect and dependence on fossil fuel [1-4], studies on the conversion of CO_2 to valuable fuel have garnered attention. Recently, enormous endeavors have been made to achieve this purpose, primarily based on some functional catalytic materials, including inorganic semiconductors [5-6], metal–organic framework (MOFs) [7], and covalent organic frameworks (COFs) [8], C_3N_4 [9]. However, many issues persist, such as low efficiency and uncontrollable selectivity during the catalytic process. The exploration of ideal catalytic materials for the highly efficient conversion of CO_2 to a single product is an urgent task. Particularly, reducing CO_2 to CH_4 fuel has great importance due to the wide application of CH_4 as fuel [10]. The conversion of CO_2 to CH_4 is a difficult task mainly due to the following two reasons. Firstly, molecular CO_2 is quite stable with a strong C=O bond, which leads to extremely high dissociation energy of around 750 kJ mol⁻¹. Secondly, to finish the whole conversion process from CO_2 to CH_4, a significant amount of H^+ must participate throughout the whole reduction reactions.

Based on the coordination catalysis theory [11], the active site on the catalyst surface has been proven to be able to activate the CO_2 molecule. Some synergistic effects from the active sites would greatly reduce the dissociation energy of CO_2 to greatly improve the catalytic activity. Besides, CO_2 adsorbance on some specific sites on the catalyst surface allows electrons to transform into CO_2 through the formed chemical bonds. Furthermore, the coordination mode (active site) on the catalyst surface is also regarded as a determining factor to control the intermediate states and govern the final products [12-13]. Therefore, understanding the process of coordination activation is of urgent interest, particularly how the dissociation energy of CO_2 can be reduced and the final product of CH_4 can be achieved.

Generally, the conventional process of CO_2 on the surface of a transition metal oxide follows several stages [14-16]. As shown in Scheme 1(a), a transition metal atom M is only considered as an adsorption site to bridge with the O site of the CO_2 molecules. At stage I, a weak interaction of M···O=C=O suggests the difficulty of CO_2 molecule activation. At stage II, a coordination mode with M···O=C=O···M prefers the formation of HCOOH. At stage III, one activated C=O bond in O=C=O will

---

*To whom all correspondence should be addressed.

be dissociated, and finally converted from CO_2 to CO. Moreover, Scheme 1b (intermediate-IV) depicts that the M atom with dangling bonds (unpaired electron) from the O vacancy interacts with the CO_2 molecule. These processes require cooperation with H^+ to reduce CO_2 from the molecule to CH_4. The activated C=O bond would easily transform into M···CHO⁻···M, and generate the C-H bond.

Ultrathin two-dimensional (2D) nanosheets have been widely employed as functional catalyst materials [16-19] owing to their extremely large surface area, plenty of exposed metal atoms, and abundant defects on the surface. Besides, an ultrathin nanosheet is regarded as an ideal catalyst model with an abundance of surface M atoms and O vacancies, which would help explore the coordination pathway at an atomic scale and for the conversion of CO_2 to CH_4. TiO_2 with different morphologies (including the TiO_2 nanosheet) is widely used as a high-efficient catalyst for the reduction of CO_2 [16, 20-21].

However, few works have reported on active site-promoted activation. In essence, Ti^{3+} is one of the most important active sites on the exposed TiO_2 surface, particularly due to its ultra-thin morphology that allows for additional Ti^{3+} active site loading. Therefore, the reduction process of CO_2 is of urgent interest to have a deeper insight into the TiO_2 nanosheet at an atomic level. Herein, we employed DFT simulations to reveal the reduction process of CO_2 on an ultrathin rutile TiO_2 (110) surface within the guideline of Scheme 1. The (110) surface is the main exposed crystal face in the rutile TiO_2 with abundant Ti^{3+} sites. Besides, our DFT simulation results also indicate that the unsaturated coordination Ti^{3+} on the active surface can provide a strong binding force to form M···CHO⁻···M, finally inducing the reduction of CO_2 to CH_4. This work can provide theoretical support to explore new efficient catalysts for the reduction of CO_2.
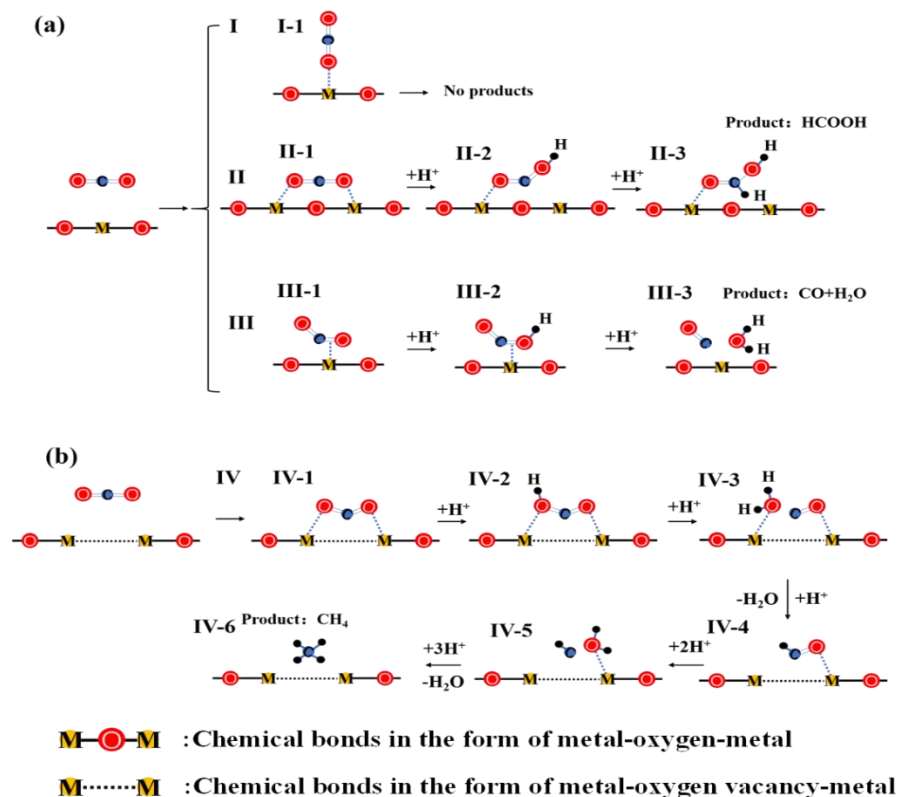
Scheme-1: Reduction process of CO_2 on the surface of the catalyst, M stands for the metal site, H^+ refers to the proton, and $-H_2O$ defines the molecule H_2O. Reduction of CO_2 on the catalyst (a) with standard coordination model, and (b) with coordination model of the O vacancy.

Experimental

CP2K [22] was employed to carry out the theoretical density functional theory (DFT) calculations. CP2K is a quantum chemistry and solid-state physics software package that can perform atomistic simulations of solid state, liquid molecular, periodic material, crystal, and biological systems in a general framework for different modeling methods. The CP2K program, which was used in the DFT mode, employs two representations of the electron density: localized Gaussian and plane wave basis sets. For the Gaussian-based (localized) expansion of the Kohn–Sham orbitals, we used a library of contracted molecularly optimized valence double-zeta plus polarization basis sets [23], and the complementary plane wave basis set had a cutoff of 400 Rydberg for the electron density. The valence electron–ion interaction was based on the norm-conserving and separable pseudopotentials of the analytical form derived by Goedecker, Teter, and Hutter [24]. The generalized gradient corrected approximation of Perdew, Burke, and Ernzerhof was adopted for GGA exchange–correlation [25-30] is adopted to relax the geometric structures. An actual grid spacing smaller than 0.04 Å^{-1} was selected to divide the reciprocal space. The criterion for structural relaxation was below 0.01 eV Å^{-1} to limit the total force on each ion. Spin polarization was considered during calculations. A convergence criterion of 10^{-6} eV was employed for electronic self-consistent cycles.

Transition state optimization was employed with the nudged-elastic band algorithm [31-32] (CINEB) based on the CP2K package. The number of inserted images used in the CINEB calculations depended on the reaction coordinates between the reactant and product. The initial (reactant) and final (product) configurations were obtained from fully converged relaxation. The number of inserted images used in the CINEB calculations depended on the reaction coordinates between the reactant and product. The criterion for the convergence of CINEB was reached when the total force on each ion was reduced to below 0.05 eV Å^{-1}.

The adsorption energy was calculated according to $E_{ads} = E_{X/slab} - [E_{slab} + E_X]$ [33], where $E_{X/slab}$ is the total energy of the slab with adsorbates in its equilibrium geometry; E_{slab} is the total energy of the bare slab; and E_X is the total energy of the free adsorbates with the liquid model being considered.

Results and Discussion

The adsorption of CO_2 on the active surfaces

According to the adsorption states of CO_2 (named as I-1, II-1, III-1, and IV-1) presented in Scheme 1, the adsorption configurations of CO_2 on the rutile TiO_2 (110) surface were correspondingly set up and displayed in Fig. 1 from (a) to (d).Ti^{3+} was exposed on the surface as active sites, and the adsorption configurations of CO_2 on TiO_2 (110) in Figs. 1 (a)(a'), (b)(b'), and (d)(d') were in line with the state of I-1, II-1, and IV-1. As described in Scheme 1, except for III-1, the folded O=C bond in O=C=O was not detected after geometrical relaxation. This suggested that the route along the process of III had difficulty in taking place on the TiO_2 (110) surface and would not be considered in future conditions.

Charge density differences for the states of I-1, II-1, and IV-1 are displayed in Figs. 1 (e) to (g). The charge is mainly transferred from the Ti^{3+} site to the O^{2-} site of CO_2. However, the charge densities of II-1 and IV-1 were denser than that of I-1, which indicates that the interactions between Ti^{3+} of rutile TiO_2 (110) and O^{2-} of CO_2 in II-1 and IV-1 were stronger than that of I-1. From the adsorption energies shown in Fig. 1(h), the adsorption energies of I-1, II-1, and IV-1 still followed the tendency of charge density differences in Figs. 1 (e) to (g). The more negative E_{ads} indicated stronger interactions between adsorptions and substrate, which followed the following order: $E_{ads\_IV-1} > E_{ads\_II-1} > E_{ads\_I1}$. Due to the rather weak adsorption energy of I-1 with only around -0.17 eV, CO_2 in I-1 was far away from the active (110) surface with inconspicuous charge transfer that resulted in little activation of the O=C bond in CO_2 without any product generated along the route I in Scheme 1. In a summary, route I and III in Scheme 1 will not be considered in future conditions based on the adsorption energy analysis. The adsorption states of II-1 and IV-1 agreed with the route of II and IV in Scheme 1. In addition, the transition state searching during the reduction process of CO_2 along the route II and IV was performed.
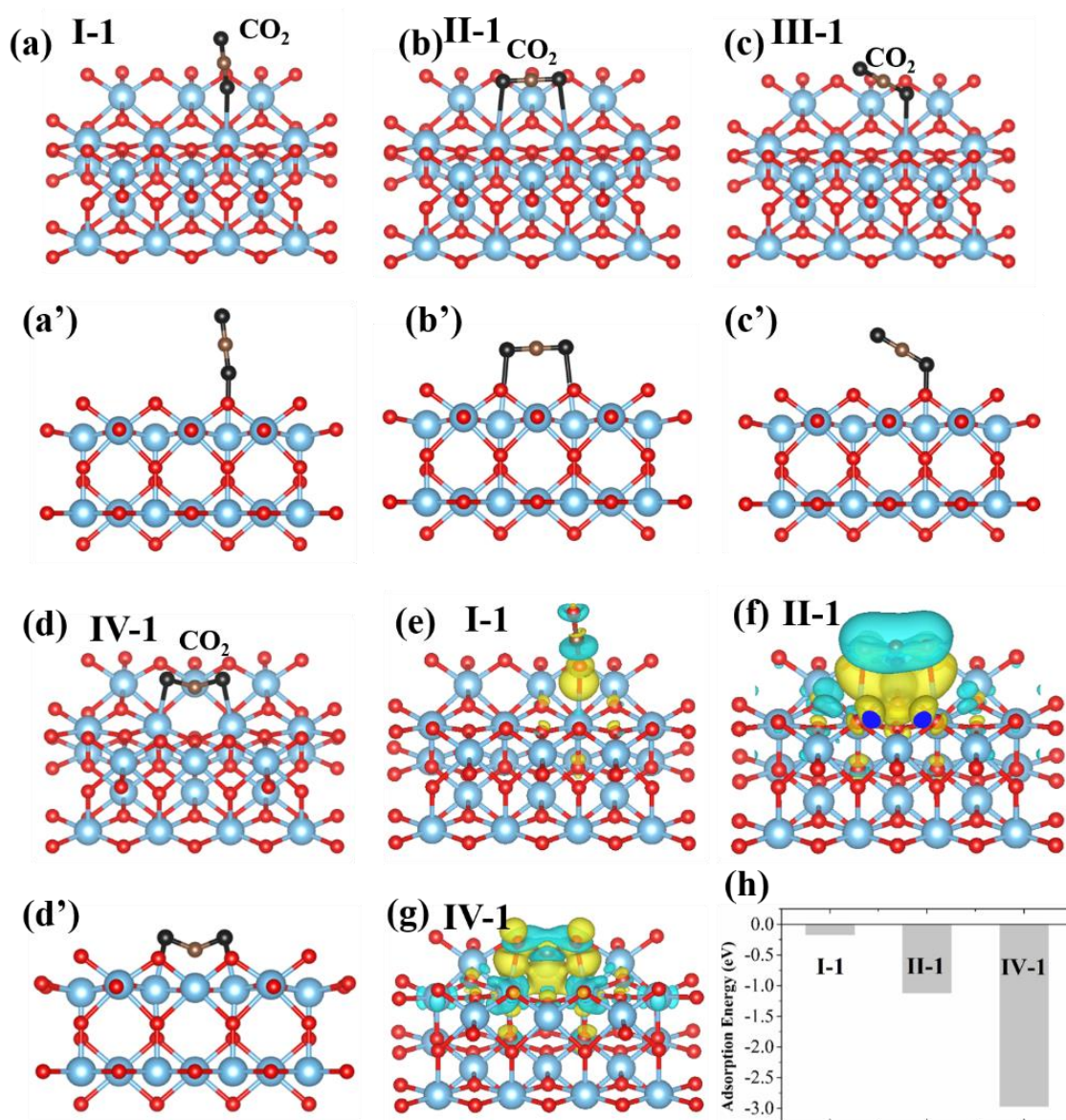
Fig. 1: Following Scheme 1, different adsorption models were correspondingly set up: (a) I-1 with a side view (a'), (b) II-1 with a side view (b'), (c) III-1 with a side view (c'), and (d) IV-1 with a side view (d'). Charge density differences for (e) I-1, (f) I-1, and (g) IV-1. (h) Adsorption energy for the state of I-1, II-1, and IV-1.
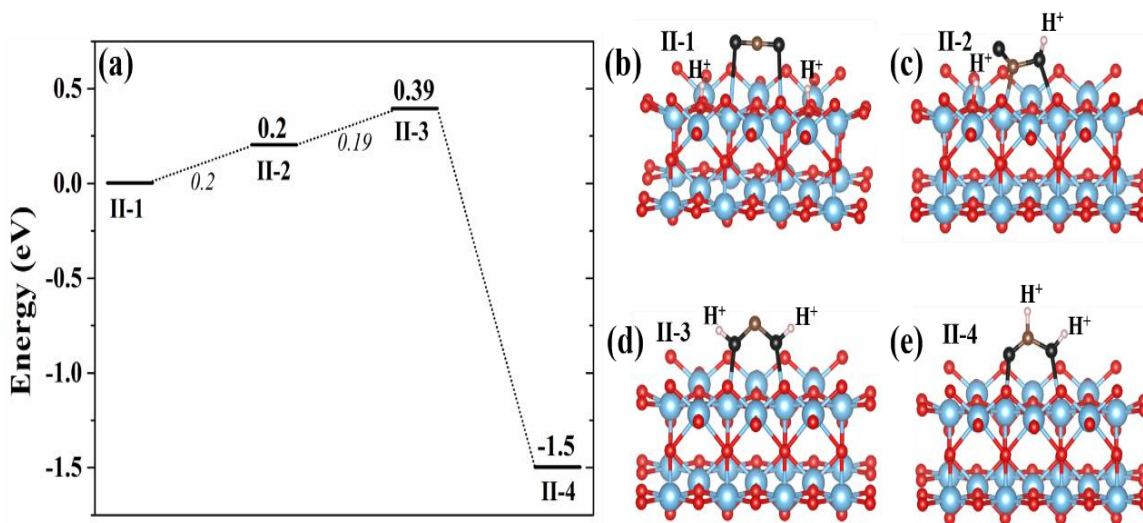
Fig. 2: (a) The energies of some intermediate states in the reduction process of CO_2 on rutile TiO_2 (110) surface along route II. The intermediate state of (b) H···O=C=O···H named as II-1, (c) H···O=C=O-H named as II-2, (d) H-O=C=O-H named as II-3, and (e) O=CH-OH named as II-4.

Reduction process of CO_2 along route II

Following the reduction process of CO_2 along route II, the energy differences of some intermediate states are displayed in Fig. 2(a). The energy of H···O=C=O···H (II-1, Fig. 2 (b)) served as a reference, in which two extra H^+ adsorbing on the O site safeguarded the uniform number of atoms in the whole reduction process. Fig. 2(c) presents the configuration of H···O=C=O-H (named II-2), in which one H^+ bridged with an O site of O=C=O-H and still left the other H^+ to bond with the O site on the rutile TiO_2 (110) surface. As the other H^+ migrated to the bond with the other O site in O=C=O-H, a new intermediate state of H-O=C=O-H was generated, as exhibited in Fig. 2 (d). When one H^+ migrated from the O site to the C site, the fuel HCOOH was produced as the final product. According to the energy difference displayed in Fig. 2(a), the energy increased with only 0.2 eV as the adsorption state transferred from II-2 to II-1. The energy increase was still limited between II-3 and II-2 with only 0.19 eV. These small energy differences indicated that the corresponding reduction process was likely to take place under the effects of thermal fluctuation. Huge energy decreasing

with -1.89 eV was detected from II-3 to II-4, which indicates that the state of II-4 was the most stable. The final product of HCOOH tended to be generated on the TiO_2 (110) surface.

To make a careful assessment of the transition states from II-3 to II-4, a CINEB simulation was carried out as follows, as displayed in Fig. 3. The activation barrier from II-3 to II-4 was as low as 0.54 eV, which mainly came from the competition adsorption of H^+ between the O and C sites in H-O=C=O-H, as shown in the transition state of Fig. 3(c). However, this small activation barrier of 0.54 eV did not significantly impede the corresponding process based on the standard Redhead analysis [34-35]. In summary, the whole reduction process from CO_2 to HCOOH (guided along route II in Scheme 1) had a high probability of finishing on the rutile TiO_2 (110) surface due to quite finite energy differences and a small activation barrier. Besides, the synergistic action of the active Ti^{3+} site and H^+ helped fix molecular CO_2 and break the strong bond of C=O in CO_2 on the (110) surface.
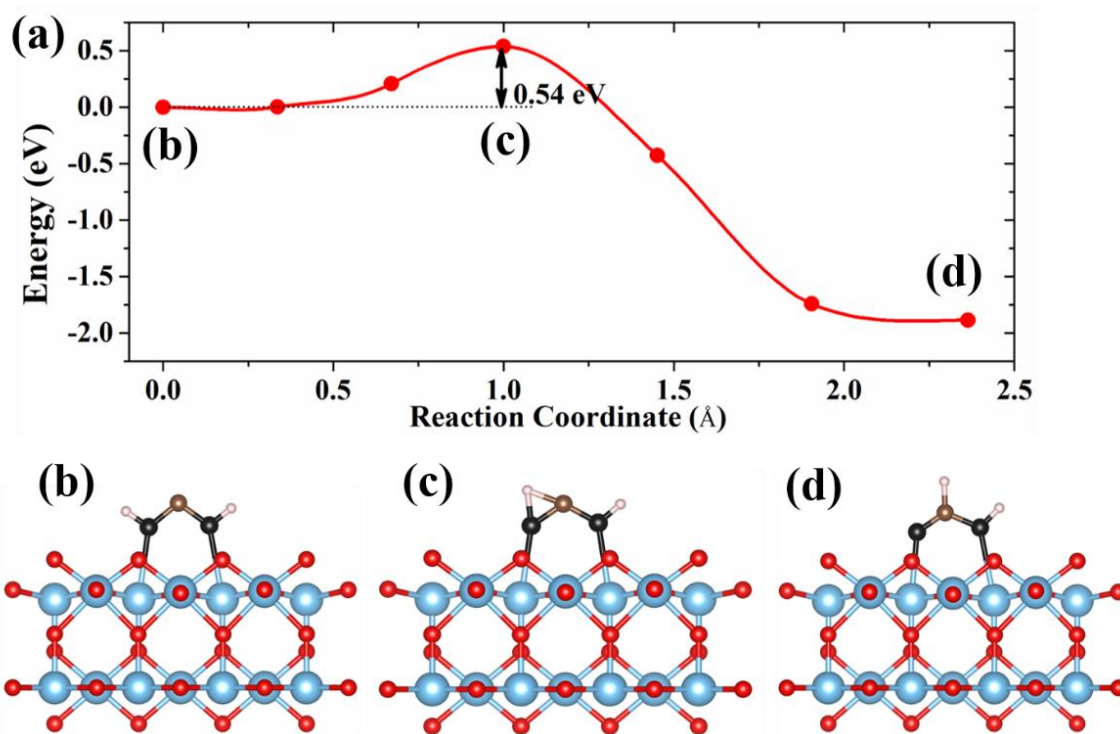
Fig. 3:   (a) Transition state (TS) searching from II-3 H-O=C=O-H to II-4 O=CH-OH based on CINEB method. The configurations of II-3, TS, and II-4 are exhibited from (b) to (c), correspondingly.
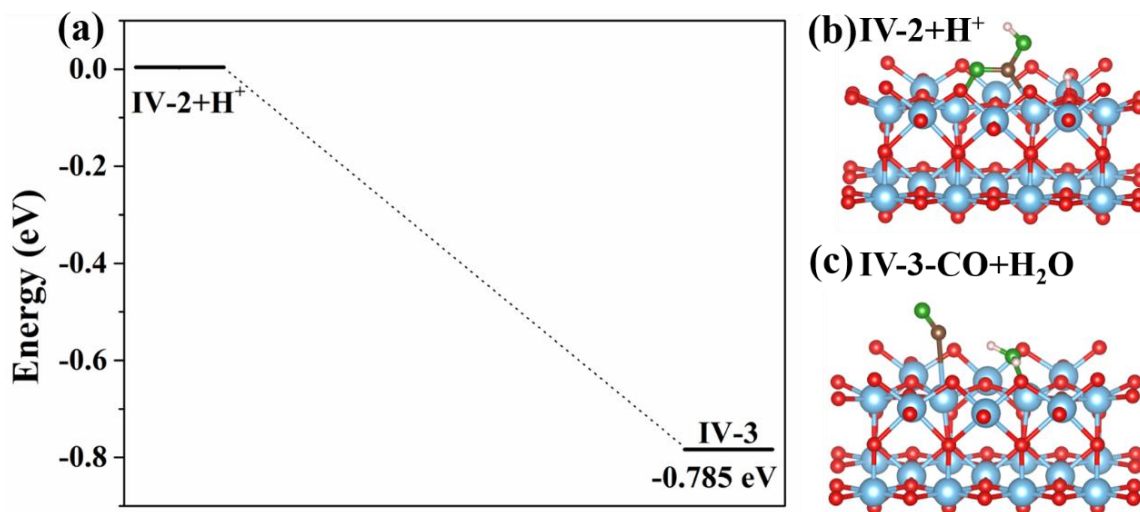
Reduction process of CO_2 along the route IV

Fig. 4:   (a) The energy difference of the state of IV-2+H^+ and IV-3 with the energy of IV-2+H^+ as the reference. The configuration of (b) IV-2+H^+ and (c) IV-3.

With the guideline along route IV in Scheme 1, molecular CO_2 (O=C=O) adsorption around the O vacancy site was still observed on the rutile TiO_2 (110) surface. In addition, two Ti^{3+} sites near the O vacancy aided in fixing O=C=O, as displayed in Fig. 1(d), thereby adding two H^+ to the active surface. One H^+ bridged with O=C=O to generate the adsorption configuration of O=C-O-H, and the other H^+ adsorbed on the O site on the rutile TiO_2 (110) surface (named as IV-2+H^+). The cooperation of H^+ on O=C=O changed the strong C=O bond into C-O-H. After relaxation, the configuration of IV-2+H^+ was obtained, as displayed in Fig. 4(b). As the other H^+ adsorbed on the O site C-OH, the C-OH bond in O=C-OH was automatically broken and directly changed into O=C+H_2O (CO plus H_2O molecules) after relaxation (Fig. 4(c)). A huge energy decrease of 0.785 eV (Fig. 4(a)) was detected as the state changed from IV-2+H^+ into IV-3-CO+H_2O. This indicates that the reduction process from O=C=O into CO+H_2O likely occurred and obeyed the defined route IV in Scheme 1.

After H_2O molecular desorbed from the surface and left the CO molecule still adsorbed on the active surface, the following reduction processes were continuously considered. To conserve the atom numbers, four extra H^+ protons and molecular CO adsorptions were taken as a reference and named IV-CO+4H^+ (Fig. 5(b)). Similar reduction processes with H^+ adsorption on the O site of C=O were considered, such as the states of H_2C-OH+H (Fig. 5(c)) and H_2C+H_2O (Fig. 5(d)). Taking the state of IV-CO+4H^+ as a reference, huge energy drops of -3.053 and -4.144 eV were also detected for H_2C-OH+H and H_2C+H_2O, respectively. Furthermore, based on the transition state (TS) search from IV-H_2COH+H to IV-H_2C-H_2O in Fig. 6(a), the associated activation barrier was determined to be only 0.27 eV, which also indicates that the C-O bond in H_2COH was easily broken and finally generated the state of H_2C+H_2O (Fig. 6(c)). At this moment, the O atoms in O=C=O were entirely deprived and left -CH_2 bridging on the surface. From the defined pathway in route IV, the whole reduction process was determined to be energetically favorable.
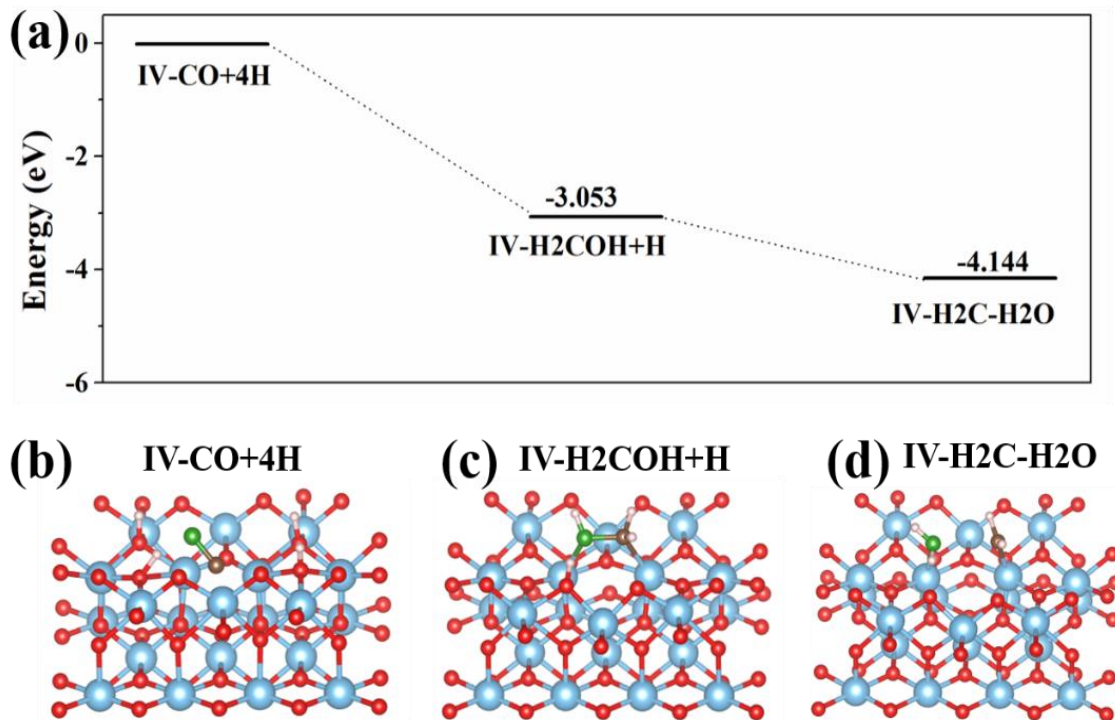

Fig. 5:   (a) The energy difference of IV-CO+4H, IV-H_2COH+H, and IV-H_2C-H_2O with the energy of IV-CO+4H as a reference. The configurations of (b) IV-CO+4H, (c) IV-H_2COH+H, and (d) IV-H_2C-H_2O.
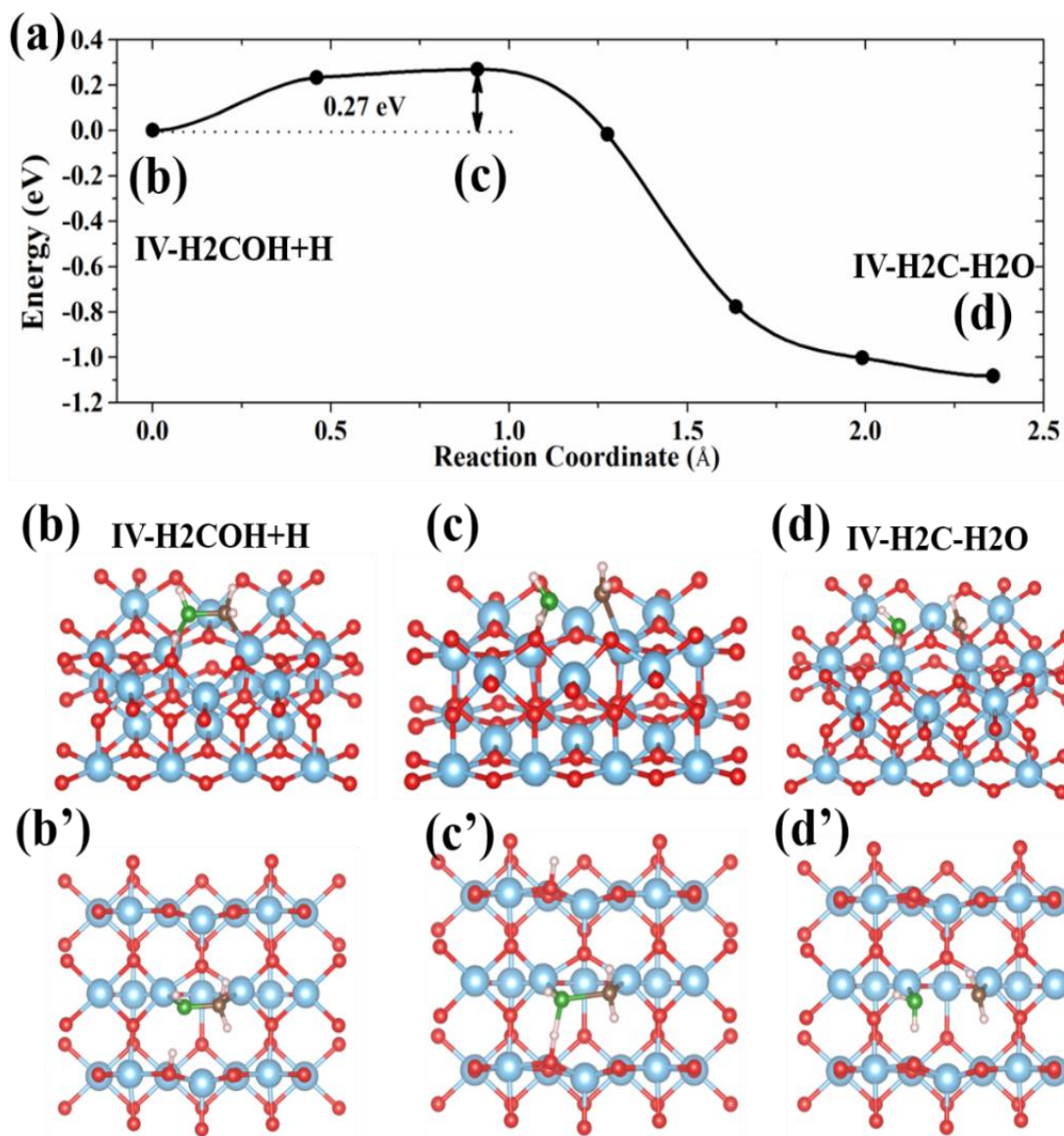
Fig. 6:   (a) Transition state (TS) searching from IV-H$_2$COH+H to IV-H$_2$C-H$_2$O based on the CINEB method. The configurations of IV-H$_2$COH+H, TS, and IV-H$_2$C-H$_2$O are exhibited from (b) side view ((b') top view) to (d) side view ((d') top view).
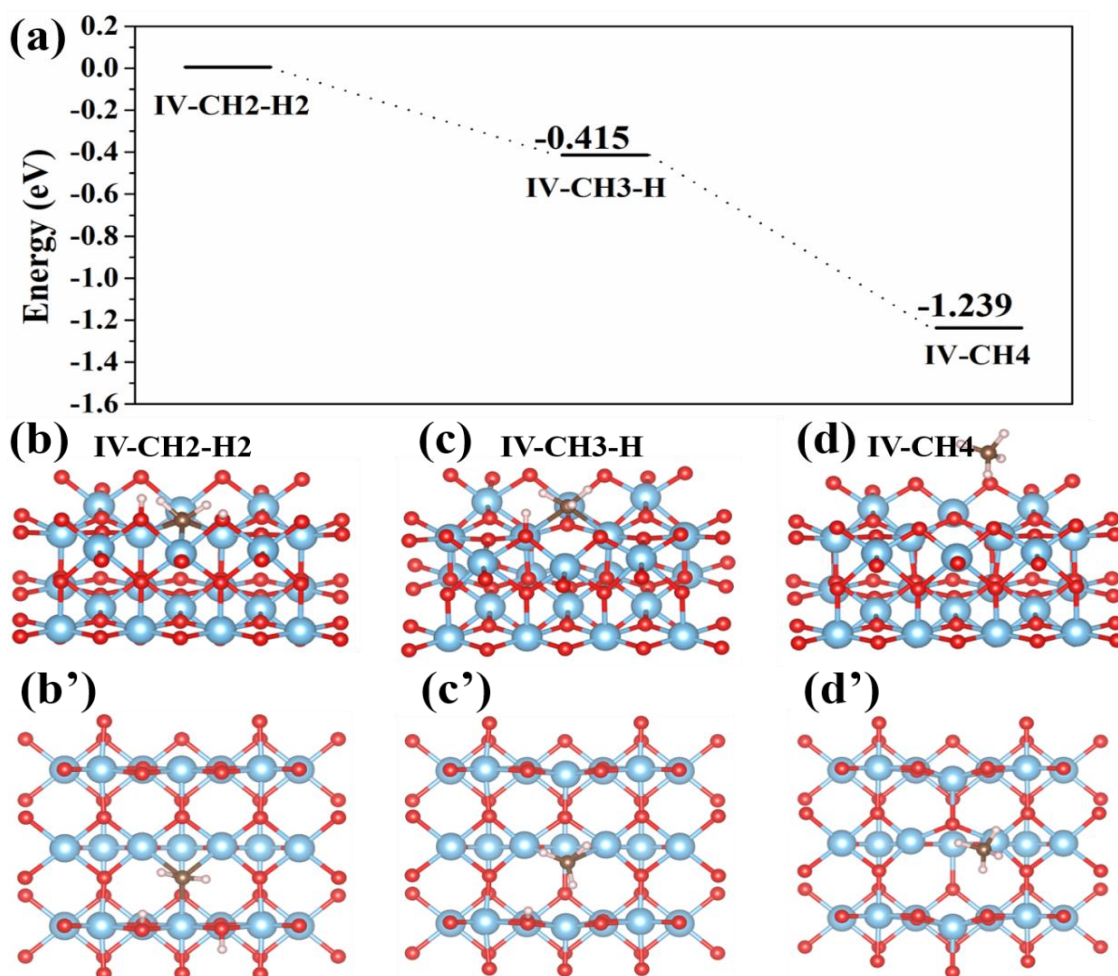
Fig. 7: (a) The energy difference of IV-CH$_2$-H2, IV-CH$_3$-H, and IV- CH$_4$ with the energy of IV-CH$_2$-H2 as a reference. The configuration of (b) side view/(b') top view of IV-CH$_2$-H2, (c) side view/(c') top view of IV-CH$_3$-H, and (d) side view/(d') top view of IV- CH$_4$.

Figs. 7(b) and 7(b') show the configuration of IV-CH$_2$-H2 with -CH$_2$ adsorbing on the surface and two H$^+$ bridging with the O site of the active surface. As H$^+$ gradually migrated from the O site to C, the configurations of IV-CH$_3$-H (Figs. 7(c), 7(c')) and IV-CH$_4$ (Figs. 7(d), 7(d')) were formed. The obvious energy drops of -0.145 eV and -1.239 eV in Fig. 7(a) also suggest that reduction by adding H$^+$ was energetically favorable. The final product of CH$_4$ was generated following route IV in Scheme 1.

Conclusion

In this study, we found that regarding the previous assumptions exhibited in Scheme 1, the reduction processes of CO$_2$ on the rutile TiO$_2$ (110) surface along I and III were difficult to achieve. By contrast, the whole reduction processes of CO$_2$ tended to finish along the routes of II and IV. The active sites of Ti^{3+} and the O vacancy on the (110) surface had important roles in adsorbing molecular CO$_2$ and had synergistic effects on breaking the strong bond of C=O in CO$_2$ on the (110) surface with the assistance of H$^+$. In route II, the energy differences, as well as the activation barrier, were limited among the various intermediate states, which resulted in generating HCOOH as final products via coordination activation. In route IV, the finite energy differences and activation barrier also safeguarded the whole reduction process from CO$_2$ to CH$_4$. As such, the coordination activation mechanism could enlighten the design of more active catalysis processes, especially considering the effects of coordination activation for the reduction of CO$_2$.

Acknowledgments

We thank LetPub (www.letpub.com) for its linguistic assistance during the preparation of this manuscript.

References:

1. C. Das Neves Gomes, O. Jacquet, C. Villiers, P. Thuéry, M. Ephritikhine and T. Cantat. A Diagonal approach to chemical recycling of carbon dioxide: Organocatalytic transformation for the reductive functionalization of CO_2. *Angew. Chem. Int. Ed.,* **51**, 187 (2012).

2. X. Li, J. Yu, M. Jaroniec and X. Chen. Cocatalysts for selective photoreduction of CO_2 into solar fuels. *Chem. Rev.*, **119**, 3962 (2019).

3. S. N. Habisreutinger, L. Schmidt-Mende and J. K. Stolarczyk. Photocatalytic reduction of CO_2 on TiO_2 and other semiconductors. *Angew. Chem. Int. Ed.*, **52**, 7372 (2013).

4. Y. Y. Birdja, E. Pérez-Gallent, M. C. Figueiredo, A. J. Göttle, F. Calle-Vallejo and M. T. M. Koper. Advances and challenges in understanding the electrocatalytic conversion of carbon dioxide to fuels. *Nat. Energy*, **4**, 732 (2019).

5. A. Razzaq, S. Ali, M. Asif and S. In. Layered Double Hydroxide (LDH) Based Photocatalysts: An Outstanding Strategy for Efficient Photocatalytic CO_2 Conversion. *Catalysts*, **10**, 1185 (2020).

6. Y. F. Xu, M. Z. Yang, B. X. Chen, X. D. Wang, H. Y. Chen, D. Bin Kuang and C. Y. Su. A $CsPbBr_3$ perovskite quantum dot/graphene oxide composite for photocatalytic CO2 reduction. *J. Am. Chem. Soc.*, **139**, 5660 (2017).

7. R. Li, W. Zhang and K. Zhou. Metal–Organic-Framework-Based catalysts for photoreduction of CO_2. *Adv. Mater.*, **30**, 1705512 (2018).

8. S. Yang, W. Hu, X. Zhang, P. He, B. Pattengale, C. Liu, M. Cendejas, I. Hermans, X. Zhang, J. Zhang and J. Huang. 2D covalent organic frameworks as intrinsic photocatalysts for visible light-driven CO_2 reduction. *J. Am. Chem. Soc.*, **140**, 14614 (2018).

9. Z. Sun, H. Wang, Z. Wu and L. Wang. g-C_3N_4 based composite photocatalysts for photocatalytic CO_2 reduction. *Catal. Today*, **300**, 160 (2018).

10. O.K. Varghese, M. Paulose, T. J. LaTempa and C. A. Grimes. High-rate solar photocatalytic conversion of CO_2 and water vapor to hydrocarbon fuels. *Nano Lett.*, **9**, 731 (2009).

11. Q. Liu, L. Wu, R. Jackstell and M. Beller. Using carbon dioxide as a building block in organic synthesis. *Nat. Commun.*, **6**, 1 (2015).

12. X. Li, Y. Sun, J. Xu, Y. Shao, J. Wu, X. Xu, Y. Pan, H. Ju, J. Zhu and Y. Xie. Selective visible-light-driven photocatalytic CO_2 reduction to CH_4 mediated by atomically thin $CuIn_5S_8$ layers. *Nat. Energy*, **4**, 690 (2019).

13. A. Kubacka, M. Fernández-García and G. Colón. Advanced nanoarchitectures for solar photocatalytic applications. *Chem. Rev.*, **112**, 1555 (2012).

14. Q. Liu, L. Wu, R. Jackstell and M. Beller. Using carbon dioxide as a building block in organic synthesis. *Nat. Commun.*, **6**, 1 (2015).

15. C. Tan, X. Cao, X. J. Wu, Q. He, J. Yang, X. Zhang, J. Chen, W. Zhao, S. Han, G. H. Nam, M. Sindoro and H. Zhang. Recent advances in ultrathin two-dimensional nanomaterials. *Chem. Rev.*, **117**, 6625 (2017).

16. Z. W. Wang, Q. Wan, Y. Z. Shi, H. Wang, Y. Y. Kang, S. Y. Zhu, S. Lin and L. Wu. Selective photocatalytic reduction CO2 to CH4 on ultrathin TiO2 nanosheet via coordination activation. *Applied Catalysis B: Environmental*, **288**, 120000 (2021).

17. S. Liang, L. Wen, S. Lin, J. Bi, P. Feng, X. Fu, L. Wu. Monolayer HNb_3O_8 for selective photocatalytic oxidation of benzylic alcohols with visible light response. *Angew. Chem. Int. Ed.*, **53**, 2951 (2014).

18. H. Wang, S. Luo, Y. Song, Y. Shi, Z. Wang, B. Guo and L. Wu. Enhanced photocatalytic hydrogen evolution over monolayer HTi_2NbO_7 nanosheets with highly dispersed Pt nanoclusters. *Appl. Surf. Sci.*, **511**, 145501 (2020).

19. Y. Song, H. Wang, Z. Wang, B. Guo, K. Jing, Y. Li and L. Wu. Selective photocatalytic synthesis of Haloanilines from Halonitrobenzenes over multifunctional AuPt/Monolayer titanate nanosheet. *ACS Catal.*, **8**, 9656 (2018).

20. J. H. Park, J. H. Kim. Selective CO_2 photoconversion on low-coordinate TiO_2. *Chem.*, **6**, 2435 (2020).

21. Ž. Kovačič, B. Likozar, M. Huš, Photocatalytic CO_2 reduction: A review of Ab initio mechanism, kinetics, and multiscale modeling simulations. *ACS Catal.*, **10**, 14984 (2020).

22. www.cp2k.org.

23. V. Vande, J. J. Hutter. Gaussian basis sets for accurate calculations on molecular systems in gas and condensed phases. *J. Chem. Phys.*, **127**, 114105 (2007).

24. S. Goedecker, M. Teter and J. Hutter. Separable dual-space Gaussian pseudopotentials. *Phys. Rev.*

B, **54**, 1703 (1996).

25. J. P. Perdew, K. Burke, and M. Ernzerhof. Generalized gradient approximation made simple. *Phys. Rev. Lett.*, **77**, 3865 (1996).

26. G. Kresse, J. Hafner. Ab initio molecular dynamics for liquid metals. *Phys. Rev. B*, **47**, 558 (1993).

27. G. Kresse, J. Hafner. Ab initio molecular-dynamics simulation of the liquid-metal–amorphous-semiconductor transition in germanium. *Phys. Rev. B*, **49**, 14251 (1994).

28. G. Kresse, J. Hafner. Ab initio molecular dynamics for open-shell transition metals. *Phys. Rev. B*, **48**, 13115 (1993).

29. P. E. Blöchl. Projector augmented-wave method. *Phys. Rev. B*, **50**, 17953 (1994).

30. G. Kresse, D. Joubert. From ultrasoft pseudopotentials to the projector augmented-wave method. *Phys. Rev. B*, **59**, 1758 (1999).

31. G. Henkelman, B. P. Uberuaga and H. Jonsson. A climbing image nudged elastic band method for finding saddle points and minimum energy paths. *J. Chem. Phys.*, **113**, 9901 (2000).

32. G. Henkelman, H. Jonsson. Improved tangent estimate in the nudged elastic band method for finding minimum energy paths and saddle points. *J. Chem. Phys.*, **113**, 9978 (2000).

33. Z. Su, M. Q. Chen, Y. Pan, Y. Liu, H. Xu, Y. Zhang and D. Long. Expediting polysulfide catalytic conversion for lithium–sulfur batteries via in situ implanted ultrafine Fe_3O_4 nanocrystals in carbon nanospheres. *J. Mater. Chem. A*, **8**, 24117 (2020).

34. P. M. Kowalski, B. Meyer, and D. Marx. Composition, structure, and stability of the rutile TiO_2 (110) surface: Oxygen depletion, hydroxylation, hydrogen migration, and water adsorption. *Phys. Rev. B,* **79**, 115410 (2009).

35. P. A. Redhead. Thermal desorption of gases. *Vacuum*, **12**, 203 (1962).